Editors' Suggestion

Inverse design of discrete mechanical metamaterials

Henrik Ronellenfitsch,[1] Norbert Stoop,[1,2] Josephine Yu,[3] Aden Forrow,[1,4] and Jörn Dunkel[1]

[1]*Department of Mathematics, Massachusetts Institute of Technology, 77 Massachusetts Avenue, Cambridge, Massachusetts 02139-4307, USA*

[2]*Institute of Building Materials, ETH Zürich, Stefano-Franscini-Platz 3, 8093 Zürich, Switzerland*

[3]*Department of Physics, Massachusetts Institute of Technology, 77 Massachusetts Avenue, Cambridge, Massachusetts 02139-4307, USA*

[4]*Mathematical Institute, University of Oxford, Andrew Wiles Building, Radcliffe Observatory Quarter, Woodstock Road, Oxford OX2 6GG, United Kingdom*

(Received 16 June 2019; published 23 September 2019)

Mechanical and phononic metamaterials exhibiting negative elastic moduli, gapped vibrational spectra, or topologically protected modes enable precise control of structural and acoustic functionalities. While much progress has been made in their experimental and theoretical characterization, the inverse design of mechanical metamaterials with arbitrarily programmable spectral properties and mode localization remains an unsolved problem. Here, we present a flexible computational inverse-design framework that allows the efficient tuning of one or more gaps at nearly arbitrary positions in the spectrum of discrete phononic metamaterial structures. The underlying algorithm optimizes the linear response of elastic networks directly, is applicable to ordered and disordered structures, scales efficiently in two and three dimensions, and can be combined with a wide range of numerical optimization schemes. We illustrate the broad practical potential of this approach by designing mechanical band-gap switches that open and close preprogrammed spectral gaps in response to an externally applied stimulus such as shear or compression. We further show that the designed structures can host topologically protected edge modes, and validate the numerical predictions through explicit three-dimensional finite-element simulations of continuum elastica with experimentally relevant material parameters. Generally, this network-based inverse design paradigm offers a direct pathway toward manufacturing phononic metamaterials, DNA origami structures, and topoelectric circuits that can realize a wide range of static and dynamic target functionalities.

DOI: 10.1103/PhysRevMaterials.3.095201

I. INTRODUCTION

Phononic metamaterials [1] offer exciting opportunities to precisely control the passage of sound waves in applications ranging from acoustic cloaking [2] and lensing [3] to art [4]. Often, the counterintuitive properties of such materials arise from gaps in their vibrational spectra, which prevent or attenuate the conduction of sound over specific frequency ranges. Recent advances in additive manufacturing techniques such as three-dimensional (3D) printing [5] and lithography [6] make it possible now to assemble and experimentally characterize geometrically complex mechanical metamaterials [7]. In parallel, insightful theoretical studies [8] have substantially improved our understanding of the effects of lattice geometry and broken symmetries on band structure, mode localization, and topological protection in phononic metamaterials [9,10]. Despite such important progress, major challenges remain regarding the inverse design of mechanical metamaterials with arbitrarily programmable spectra and modes. In particular, the systematic design of highly amorphous, dynamically tunable structures that allow the controlled switching [11–15] between gapped and ungapped states remains an important problem. Here, we introduce and demonstrate a theoretical and computational framework to solve static and dynamic inverse design tasks for a broad class of discrete mechanical metamaterials.

The problem of designing ordered and disordered materials with desired spectral properties has a long and rich history [1,8,9,16,17]. In the context of modern metamaterials, engineered band gaps were studied first in optics using approaches ranging from direct shape-optimization in periodic [18] and disordered systems [19] to the tuning of hyperuniform geometries [20,21] to realize desired electromagnetic absorption and transmission spectra. Over the past years, the underlying concepts were generalized to acoustic band-gap engineering through the exploitation of locally resonant units [8], hierarchical self-similar lattices [22], gyroscopic materials with topologically protected modes [23,24], and topology optimization of continuous materials [16,17,25]. The research in these areas has identified resonances [26] and impedance mismatch between different material components [27] as the two primary mechanisms underlying band-gap formation. In parallel, recent work on quantum [28] and quantumlike [29] systems showed that disorder can promote band-gap formation. Building on these complementary insights, the inverse design approach described below achieves programmable band gaps and mode localization by optimizing the linear physical response, typically yielding highly disordered unit cells.

Our algorithmic framework is based on a discrete network representation of the underlying mechanical structure, rendering it equally applicable to a broad range of ordered and disordered [30–35] systems. Compared with earlier works that focused on the direct numerical tuning of spectral band gaps in continuum [16] and discrete [36] materials through

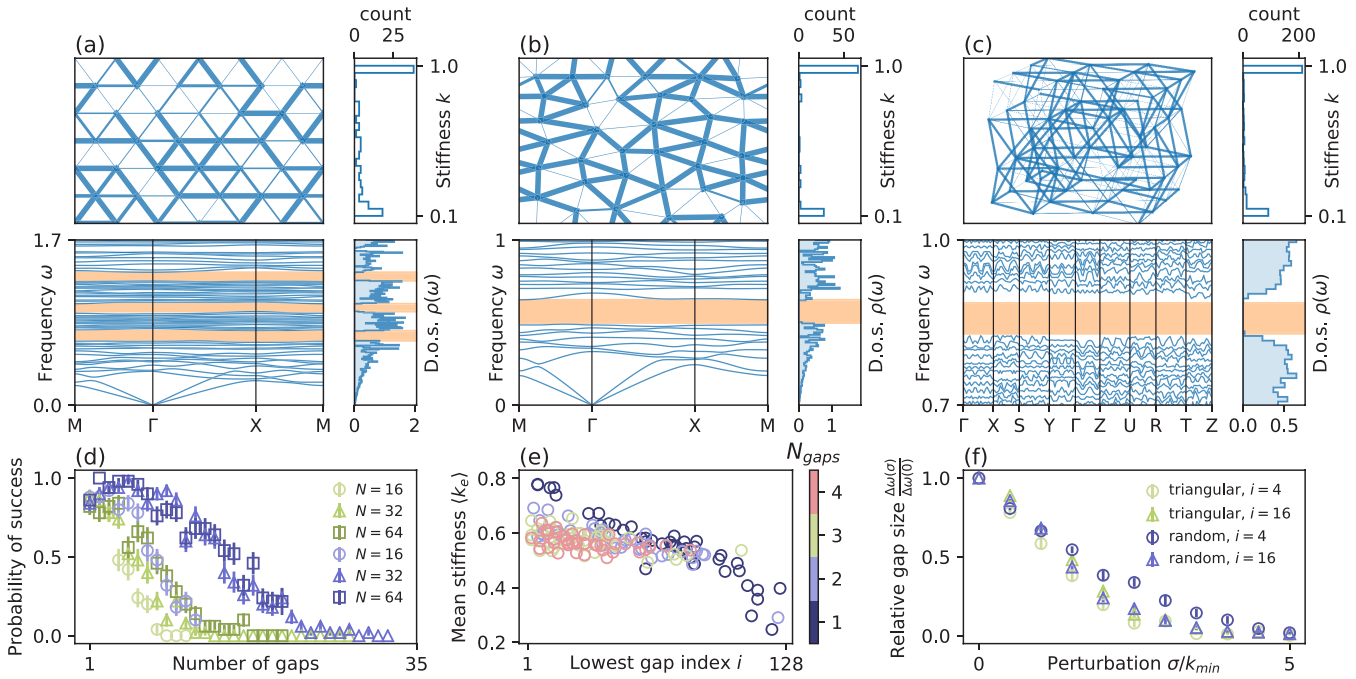

FIG. 1. Designing band gaps in 2D and 3D phononic networks by linear-response optimization (LRO). (a) Triangular 6×6 unit cell of a 2D periodic network with three tuned band gaps (orange). In the optimized network, most springs have stiffness values at the boundaries of the permitted interval [0.1,1]. The band structure was computed over the points $\Gamma = (0, 0)$, $M = (0, \pi/b)$, $X = (\pi/a, \pi/b)$, where a, b are the dimensions of the rectangular unit cell in the x and y directions. (b) Randomized 2D Delaunay network unit cell with one tuned gap (Movie 1 [38]). The bimodal stiffness distribution yields a stiff scaffold network with soft "holes," realizing impedance mismatch. (c) A single gap programmed into a 3D tetrahedral network. The band structure was computed over the points for the orthorhombic unit cell from Ref. [39], and the density of states (D.o.s.) $\rho(\omega)$ was calculated from a uniform discretization of the Brillouin zone with 51×51 samples. In all network plots of (a)–(c), the linewidth is proportional to the spring stiffness, with stiffer springs corresponding to thicker lines. (d) The probability of successfully tuning a predetermined number of gaps into an N-vertex unit cell is significantly higher for networks with amorphous topology (blue) than for triangular grids (green). Each data point is an average over 50 random choices for a fixed number of target gaps; error bars indicate standard deviation of success probability. (e) The mean stiffness is negatively correlated with the index of the lowest tuned gap. As the number of gaps increases, the stiffness distribution becomes less binary and less correlated to the gap position. We show data for an 8×8 triangular grid, but randomized topologies behave similarly. (f) Gap robustness is independent of gap position and network topology. For both triangular and amorphous unit cells with a single gap at mode index i, the addition of zero-mean Gaussian noise with variance σ to the stiffnesses causes a decrease in the gap size as $\sigma \to k_{\min}$.

topology optimization, the indirect response-optimization approach pursued here offers two essential advantages: First, conceptually it enables an interpretation of the gapped networks as response-minimized metamaterial structures. Second, computationally the scheme can be easily combined with efficient gradient-based methods. The method is not restricted to the commonly considered low-lying band gaps in highly symmetric structures, but instead allows the placement of one or more band gaps at nearly arbitrary positions in the spectrum (Fig. 1). We will show how these facts can be used to design phononic switches with prescribed spectral structure under different global deformations (Fig. 2). To connect with experiments, we will also demonstrate through 3D finite-element (FE) simulations for continuum elastica with realistic material parameters that bond bending alone can suffice to capture and tune the dynamics of continuum elastic networks (Fig. 3). Our discussion concludes by showing that the response-optimized networks can host protected chiral edge modes, thus enabling the inverse design and precise control of topological metamaterial properties (Fig. 4).

II. THEORY AND RESULTS

A. Discrete mechanical networks

The inverse design algorithm described below optimizes the linear response over a set of experimentally tunable system parameters. While the approach generalizes to arbitrary dynamical systems that can be linearized in the neighborhood of fixed points, we focus here on discrete mechanical networks consisting of n identical point masses $m_v = m$ connected by springs with stiffnesses $\{k_e\}$, where v is a vertex and e is an edge of the network. The elastic energy of the network reads

$$V = \frac{1}{2} \sum_e k_e \left(\ell_e - \ell_e^{(0)}\right)^2, \tag{1}$$

where k_e is the stiffness of spring e, ℓ_e is its length, and $\ell_e^{(0)}$ is its rest length. In this case, we are interested in programming spectral properties by optimizing over the set of spring constants $\{k_e\}$. To linear order, the dynamics of the network near the equilibrium configuration is given by

$$m\,\ddot{\mathbf{u}} + K\mathbf{u} = 0, \tag{2}$$

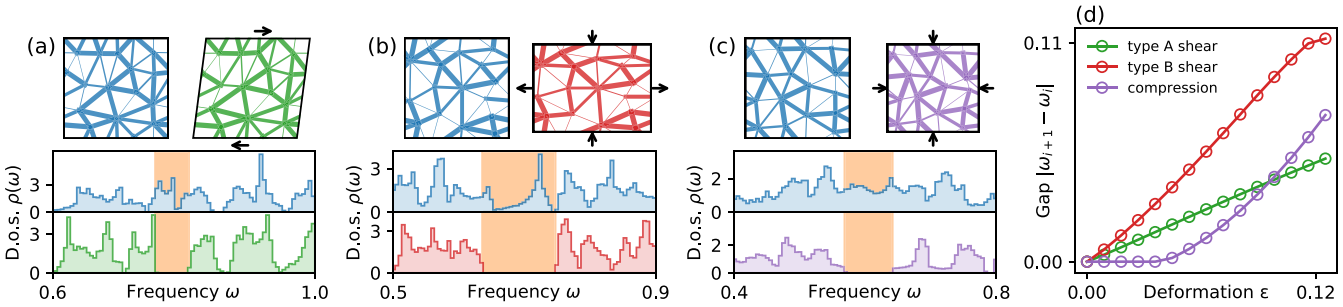

FIG. 2. Phononic metamaterial switches with unit cells possessing random topologies. (a) Network designed to open a band gap when global type A shear in the x direction ($x \mapsto x + \varepsilon y$, $y \mapsto y$, $\varepsilon = 0.125$) is applied (Movie 2). The gapless unstrained and gapped strained configurations can be seen in the density of states $\rho(\omega)$. (b) Network designed to open a gap under global type B shear [$x \mapsto (1+\varepsilon)x$, $y \mapsto (1-\varepsilon)y$, $\varepsilon = 0.125$]; see Movie 3. (c) Network designed to open a gap under global compression [$x \mapsto (1-\varepsilon)x$, $y \mapsto (1-\varepsilon)y$, $\varepsilon = 0.125$]; see Movie 4. For global compression, most spring lengths decrease, so that the second term in Eq. (A3) reduces all excitation frequencies. In contrast, for global shear, some springs lengthen while others are compressed, so that the excitation frequencies remain roughly identical. (d) The gap widths $|\omega_{i+1} - \omega_i|$ increase with the magnitude ε of the applied deformations in (a)–(c). The linear approximation for the deformed equilibrium breaks down past $\varepsilon \approx 0.125$. In all cases, the target deformation was $\varepsilon = 0.2$. Gap sizes were computed by discretizing the entire Brillouin zone using 51×51 samples.

where $\mathbf{u} = (u_v)$ is the vector of mass displacements and $K = QkQ^\top$ is the stiffness matrix, with k the diagonal matrix of individual spring stiffnesses and Q the compatibility matrix encoding the relative geometric relationships between the masses (Ref. [37] and the Supplemental Material [38]). Equation (2) can be simplified further by expanding into eigenmodes defined by the relation $K\mathbf{u}_i = m\omega_i^2 \mathbf{u}_i$, where the set $\{\omega_i\}$ constitutes the spectrum of excitation frequencies. The goal of the spectral optimization is then to construct networks with spring constants $\{k_e\}$ that realize a desired frequency spectrum $\{\omega_i\}$. Specifically, to achieve a reduced acoustic response, we would like to place large gaps between predetermined consecutive eigenvalues ω_i.

B. Response optimization

To design one or more spectral gaps at desired locations in the spectrum, we formulate a linear-response optimization (LRO) scheme that creates suitable impedance mismatches

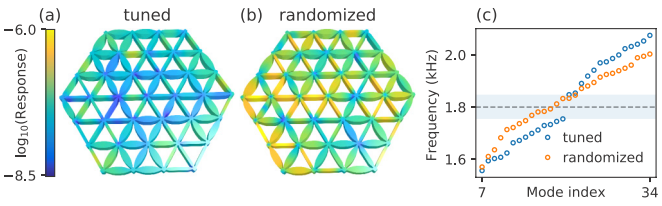

FIG. 3. Spectral gap design for continuum elastic networks. (a,b) 3D renderings of two continuum Styrodur networks (diameter ≈ 17 cm, thickness 1 cm) studied in finite-element (FE) simulations (Appendix). The color represents the in-plane harmonic response amplitude $|G_{0j}|$, where the finite elements j respond to harmonic forcing of the element 0 at the center of the network with amplitude $(1, 1, 0)/\sqrt{2}$ at the midgap frequency $\omega = 1.8$ kHz. The response of the tuned network (a) is significantly smaller than that of the network (b) with randomly permuted stiffnesses. (c) FE modes for the tuned network (a) exhibit a substantial spectral gap (blue). The gap vanishes for the network (b) with randomly permuted stiffnesses (orange).

(Fig. 1). Unlike brute-force [40] optimization (see Ref. [38]), the LRO framework yields a differentiable objective function and is equally applicable to undeformed and deformed networks (Fig. 2). The linear response to harmonic forcing $\mathbf{F}e^{i\omega t}$ is given by

$$\mathbf{u}(t) = e^{i\omega t} G(\omega; k)\mathbf{F}, \tag{3}$$

where the response function is

$$G(\omega; k) = (-m\omega^2 \mathbb{1} + K)^{-1}.$$

The time-averaged covariances of the real vertex responses are

$$C_{vv'}(\mathbf{F}) = \tfrac{1}{2}\langle \mathrm{Re}\,(u_v(t))\,\mathrm{Re}\,(u_{v'}(t))\rangle_t,$$

where $\mathrm{Re}(\cdot)$ is the real part of a complex number. Plugging in Eq. (3) and explicitly performing the time average over a period $T = 2\pi/\omega$, we find the matrix expression

$$C(\mathbf{F}) = G(\omega; k)\mathbf{F}\mathbf{F}^H G(\omega; k)^H, \tag{4}$$

where the superscript H denotes the Hermitian transpose. The strength of each node's response at frequency ω is encoded in the diagonal entries. We now average Eq. (4) further over an ensemble of independent, identically distributed random forcings $\mathbf{F}$ with covariances $\langle \mathbf{F}\mathbf{F}^H\rangle_{\mathbf{F}} = \mathbb{1}$. Using linearity of the matrix product, we obtain

$$\langle C(\mathbf{F})\rangle_{\mathbf{F}} = G(\omega; k)\underbrace{\langle \mathbf{F}\mathbf{F}^H\rangle_{\mathbf{F}}}_{=\mathbb{1}} G(\omega; k)^H. \tag{5}$$

Summing over the diagonal of $\langle C(\mathbf{F})\rangle_{\mathbf{F}}$ yields

$$R(\omega; k) = \mathrm{tr}(G(\omega; k)G(\omega; k)^H), \tag{6}$$

where $\mathrm{tr}(\cdot)$ denotes the matrix trace. Equation (6) is equivalent to the squared real network response $\frac{1}{2}\sum_v \langle\langle \mathrm{Re}(u_v)^2\rangle\rangle$, where $\langle\langle\cdot\rangle\rangle$ denotes an average over both the period $T = 2\pi/\omega$ and the forcing ensemble. Since Eq. (6) is averaged over forcings, it depends only on the spectrum and not on the eigenmodes, and thus it can be used to tune spectral properties indirectly. As an instructive example, consider a system with unit mass and only two eigenvalues at $\omega_{1,2}^2$. The minimum

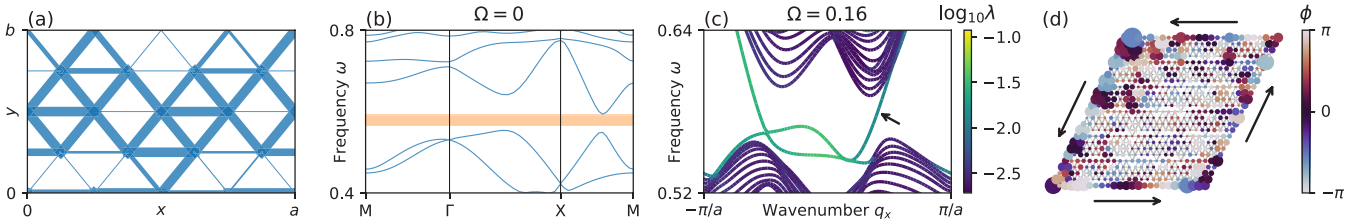

FIG. 4. Protected chiral edge modes in designed networks. (a) Designed gapped network on a triangular lattice. (b) Gapped band structure of the network from (a) in the symmetry-unbroken state ($\Omega = 0$, Chern invariant $C = 0$). (c) Chiral protected edge bands (arrow) in the topological phase ($\Omega = 0.16$, Chern invariant $C = 1$) for a ribbon with 12 open-boundary unit cells in the y direction and periodic boundary conditions in the x direction. Color corresponds to the mode localization ratio $\lambda = \sum_i u_i^4/(\sum_i u_i^2)^2$. Each of the two bands corresponds to chiral modes localized on either side of the finite ribbon. The topological phase transition occurs at $\Omega_c \approx 0.08$. (d) Localized chiral edge response to forcing in the lower left corner in a finite sample network with 6×6 unit cells. Circle size corresponds to the norm $\|\mathbf{u}_i\|^2$ of the linear response at long times, while color corresponds to the response phase.

of $R(\omega) = (\omega_1^2 - \omega^2)^{-2} + (\omega_2^2 - \omega^2)^{-2}$ occurs at $\omega_*^2 = (\omega_1^2 + \omega_2^2)/2$ with the value $R(\omega_*) = 8(\omega_2^2 - \omega_1^2)^{-2}$, inversely proportional to the gap width. Thus, minimizing the response Eq. (6) at a frequency between two eigenvalues will maximize the gap width. The above framework can be easily adapted to other classes of forcing ensembles, allowing additional optimization for application-specific input correlations $\langle \mathbf{F}\mathbf{F}^H \rangle$ [41].

C. Periodic structures

The generalization to periodic crystals is straightforward in a Bloch basis, taking the lattice Fourier transform [37] of the above relations (see Ref. [38]). In this case, the trace in Eq. (6) is replaced by a sum of traces over the response functions $G_\mathbf{q}$ at each wave vector $\mathbf{q}$ in the first Brillouin zone of the reciprocal crystal lattice. The Fourier transformed eigenmode equation is then $\hat{K}(\mathbf{q})\hat{\mathbf{u}}_i(\mathbf{q}) = m\omega_i^2(\mathbf{q})\hat{\mathbf{u}}_i(\mathbf{q})$. To numerically tune a gap between ω_i and ω_{i+1} at wave vector $\mathbf{q}$, we minimize the objective function

$$\mathcal{L}_i(\mathbf{q}; k) = R\Big(\sqrt{\tfrac{1}{2}\big(\omega_i^{(0)}(\mathbf{q})^2 + \omega_{i+1}^{(0)}(\mathbf{q})^2\big)}; k\Big), \tag{7}$$

where the frequencies $\omega_i^{(0)}$ are evaluated at the initial stiffness guess $k_e^{(0)}$. To tune multiple gaps at band indices $\mathcal{I} = \{i_1, \ldots, i_n\}$, we sum up the contributions from the individual bands and minimize $\mathcal{L}_\mathcal{I}(\mathbf{q}; k) = \sum_{i\in\mathcal{I}} \mathcal{L}_i(\mathbf{q}; k)$. Compared with direct gap optimization schemes [40], our LRO objective in Eq. (7) has the benefit of being fractional-linear in k and hence differentiable with respect to k as long as all involved matrix inverses exist. Thus, it can be efficiently minimized with derivative-based optimization algorithms (Appendix). These algorithms generally converge to one of potentially many local minima. The optimized networks presented below are based on random initial conditions and as such correspond to numerically determined local minima. We generally found that this basic approach is sufficient for designing large gaps at the desired positions. In principle, it is straightforward to combine the LRO scheme with computationally more costly global optimization techniques such as simulated annealing. The numerical results below demonstrate, however, that local optimization schemes can yield satisfactory network designs for many practical applications.

D. Band-gap tuning of 2D and 3D networks

The discrete LRO framework is equally applicable to regular and amorphous network topologies in two as well as in three dimensions. In the examples shown in Figs. 1(a)–1(c), we optimized spring constants k_e over the range [0.1,1] to create one or more band gaps at predetermined positions in the acoustic spectrum. Sufficiently large networks can support a substantial number of tuned gaps [Fig. 1(d) and Ref. [38]]. The characteristics of the final gap-optimized structures do not significantly depend on the base network topology. As a general design rule, the distribution of stiffness values k_e in the optimized networks becomes bimodal and peaked at the interval boundaries [Figs. 1(a)–1(c)]. Intuitively, this means that the LRO algorithm can generate impedance mismatch between high- and low-stiffness components. While such impedance mismatch appears to be the predominant mechanism of gap formation in our designed networks, local resonances can occur as well (see Ref. [38]). At higher gap frequencies, the relative proportion of stiff to weak bonds changes such that the mean stiffness decreases independent of the unit-cell size [Fig. 1(e)], leading to increasingly disordered network patterns (see Ref. [38]). Thus, low-lying gaps are realized by large high-stiffness regions with low-stiffness inclusions, whereas high-lying gaps are realized by large low-stiffness regions with high-stiffness inclusions.

E. Regular versus amorphous network topologies

A practically important question is how many gaps a given network can support. To explore this question systematically, we attempted to tune up to 32 gaps at random frequencies into more than 6000 networks with different unit-cell sizes and base topologies. Starting from uniform random initial conditions $k_e \in [0.1, 1]$, we estimated the success probability $P[\min_\mathbf{q} \omega_{i+1}(\mathbf{q}) > \max_\mathbf{q} \omega_i(\mathbf{q})$ for all gaps $i]$ by explicitly computing the actual final gap sizes at $4 \times 4 = 16$ different sampling points in the Brillouin zones. As expected, we found that larger unit cells can support more gaps [Fig. 1(d)]. Interestingly, however, it is easier to implement a relatively larger number of gaps when the unit cell has randomized vertex positions [Fig. 1(d)]. The algorithm for constructing these randomized unit-cell networks relies on a Delaunay triangulation (Appendix). Recent work [33,34] showed that amorphous networks are better suited for tuning static elastic

properties than regular lattices. Our results indicate that the same is true for the inverse design and control of dynamical properties such as sound transmission.

F. Robustness

Notwithstanding the recent major technological advances [5,6], fabrication of discrete metamaterials can be expected to introduce small-to-moderate deviations from the optimal network structure. To demonstrate the robustness of the inversely designed networks, we tuned a single gap at different positions into the frequency spectrum of networks with different unit-cell topologies. Thereafter, we perturbed the optimized stiffnesses by adding normally distributed noise (mean 0, standard deviation σ), and we computed the gap size for the perturbed network. Independent of the specific gap position and network topology, we found that the gap size decreases as σ increases, roughly halving in size as σ approaches the lower stiffness bound [Fig. 1(f)]. This implies that the low-stiffness components are essential for the realization of both high-lying and low-lying gaps.

G. Designing phononic switches

Going beyond basic band-gap tuning, a practically important challenge is the inverse design of metamaterials that adjust their spectra on-demand in response to an external control stimulus [11,12]. We now demonstrate how the above LRO framework can be adapted to design phononic switches that can selectively open and close spectral gaps at preprogrammed frequency ranges/band indices and stimuli (Fig. 2). As the switching mechanisms we choose global deformations, which have been used previously to induce and control gaps [13–15]. The combination of nonaffine network response and nonzero spring tensions in the strained equilibrium changes the elastic energy and therefore the vibrational spectrum [see Eq. (A3)]. Our LRO implementation tunes the deformed and undeformed spectra independently. More precisely, the deformed stiffness matrix K_{def} of a spring network under a global deformation $\Gamma : \mathbf{x} \mapsto \Gamma\mathbf{x}$ can be found to lowest order by computing the strained equilibrium positions of all nodes from the linear dynamics Eq. (2), and then expanding the nonlinear Eq. (1) around the strained equilibrium, removing all linear terms [Eq. (A3)]. From an algorithmic perspective, switch tuning falls into the class of multiobjective optimization problems, which means that, in general, there exists not a single optimal solution but instead a Pareto front of optimal tradeoffs between the individual objectives [42]. Here, we parametrize the problem of simultaneously tuning a gap in the deformed state and no gap in the undeformed state using a no-preference method by considering the scalar least-squares problem,

$$\mathcal{L}_{\mathrm{switch}}(k) = R_{\mathrm{def}}(\omega^{(0)}; k)^2 + \alpha[R(\omega^{(0)}; k) - \beta R^{(0)}]^2, \quad (8)$$

where $R^{(0)}$ is the response of the undeformed initial network, $R_{\mathrm{def}}(\omega^{(0)}; k)$ is the response of the deformed network, and $\alpha \in \{0, 1\}$. The parameter β controls the desired response of the undeformed network. Equation (8) is minimized in three passes. First, we set $\alpha = 0$, creating a network with a large gap in the deformed state. Generically, this gap persists when the deformation is switched off, only decreasing in size. This persistence is mitigated by running two additional passes with $\alpha = 1$, always feeding in the result of the previous optimization as an initial guess for the next and recomputing $\omega^{(0)}$ and $R^{(0)}$, leading to a stepwise increase of the response in the undeformed state while retaining low response in the deformed network. The value of β such that the network possesses a closed band structure in the undeformed state and a spectral gap in the deformed state is found by a parameter search, and generally lies between $5 \lesssim \beta \lesssim 25$. Examples of phononic band gap switches controlled by the two types of shear transformations and compression are shown in Fig. 2 and Movies 2–4 in the Supplemental Material [38].

III. DISCUSSION

A. Continuum elastica

Macroscopic real-world elastic networks generally exhibit behavior more complex than pure stretching. Elastic rods can also bend and twist [43], and hingelike connections can significantly influence the total elastic response. Generalizing the above ideas, we studied the influence of bending modes and hinges on spectral network design. Through a direct comparison with FE computations, we found that these two effects suffice to design realistic 3D metamaterial dynamics, as twisting is negligible in the low-frequency regime. Our extended 2D network model treats bending and hinge stiffnesses on the same footing by introducing a local preferred relative orientation for elastic rods [44] that are linked by a joint node (see Ref. [38]). Assuming stiff hinges, angular deviation from the preferred orientation is penalized at each node, and bond bending is modeled by inserting an additional node at the center of each bond. As planar continuum realizations of these idealized 2D networks, we performed FE simulations of discrete mechanical metamaterials consisting of small disks connected by rods of different in-plane diameter (Fig. 3; see Ref. [38]). The rods are tapered toward their ends to ensure similar elastic properties near the hinges. The disk-rod networks are extruded in the direction normal to their plane to obtain centimeter-thick quasi-2D material structures [Figs. 3(a) and 3(b)], which can be 3D printed or cut out of a slab of elastic material. Considering typical Styrodur parameters, we matched the effective elastic constants of the idealized 2D network model to those of the 3D FE model (Appendix). The reduction to the 2D model for band-gap design is made possible by the fact that, for sufficiently thick 3D materials, the spectrum is divided into in-plane and out-of-plane modes. Since in-plane and out-of-plane dynamics are approximately decoupled in this regime, it suffices to optimize the spectral gaps associated with these in-plane modes (see Ref. [38]). By tuning a low-frequency spectral gap into the 2D network and mapping back onto the full 3D FE model [Fig. 3(a)], we find that the gap remains highly conserved in the FE mode spectrum [Fig. 3(c), blue circles]. In contrast, a control network [Fig. 3(b)] obtained by randomly permuting the edges of the optimized network loses the gap [Fig. 3(c), orange circles]. As a consequence, the gapped 3D continuum network exhibits a significantly reduced response when the center node is forced at midgap frequency [Figs. 3(a) and 3(b)]. This

demonstration illustrates the vast practical potential of the LRO approach with regard to the inverse design of complex 3D metamaterial functionalities.

B. Topologically protected modes

Topological mechanics offers a powerful framework for the control of phononic excitations. Topologically protected phonons localized at the edges of gapped mechanical materials have been studied extensively in special lattices [23,24,29,45,46] and in random networks [28,47]. Here, we demonstrate that our designed networks can harbor such modes as well. Inverse design thus promises precise control of topological materials and may pave the way to fully programmable topology. Specifically, we consider 2D Chern insulators, originally discovered through the quantum Hall effect, in which protected modes arise through the breaking of time-reversal invariance. A mechanical Chern material was realized recently with active gyroscopes [23,24]. We focus on the direct analog of Hall insulators, breaking time-reversal symmetry by rotating a gap-tuned network about an axis perpendicular to it [48]. The resulting Coriolis force plays the role of an external magnetic field. To linear order in the rotation frequency Ω, the equations of motion read

$$m\,\ddot{\mathbf{u}} + 2m\,\boldsymbol{\Omega} \times \dot{\mathbf{u}} + K\mathbf{u} = 0, \tag{9}$$

where $\boldsymbol{\Omega} \times \mathbf{x} = (-\Omega\, x_2, \Omega\, x_1)$ in the 2D plane. By increasing the rotation rate Ω, a 2D network with designed band gap [Fig. 4(a)] can be driven through a topological phase transition. The initially open gap [Fig. 4(b)] closes at some finite $\Omega = \Omega_c$, and then reopens in a topological phase with nonzero bulk Chern invariant $C = 1$, revealing a localized band of protected edge modes in the gap [Fig. 4(c)]. In finite samples, the nontrivial topology leads to the appearance of robust, protected edge modes allowing unidirectional transport of phonons along the sample boundary [Fig. 4(d)], with chirality controlled by the sign of Ω. Although not every tuned gap can be made topological in this manner, we observed in test simulations that topological transitions occur if the original gap in the trivial regime $\Omega = 0$ exhibits a "Mexican hat" shape, as seen in Fig. 4(b). This distinctive shape is indicative of a band inversion process, which has been implicated in mechanical topological insulators before [49]. According to our numerical tests, this feature might also provide a useful indicator for potential topological transition in networks with designed band gaps. Altogether, our results suggest that topological mechanical materials could be programed to exhibit protected modes at almost any frequency, gap size, and chirality by tuning the basic building blocks of the underlying network.

IV. CONCLUSIONS

We showed that linear-response optimization (LRO) provides a flexible and efficient algorithmic framework for the inverse design of discrete elastic metamaterials with desirable spectral properties. Notably, LRO opens a path toward developing and exploring materials with amorphous unit cells, which appear capable of hosting a significantly larger number of programmable frequency gaps than their more commonly studied highly symmetric counterparts (Fig. 1). Furthermore, LRO makes it possible to rationally design mechanical systems with switchable band structure that can be controlled through external deformations (Fig. 2). Disordered base structures are particularly promising candidates in this context, because their nonaffine responses facilitate large spectral differences between deformed and undeformed material configurations. Another intriguing prospect is the inverse design of topological materials with highly controllable mode protection (Fig. 4).

The LRO approach developed here can be easily adapted to impose desired band gaps at different selected positions in the Brillouin zone, or to realize more complex spectral features such as degenerate points. While the present study focused on optimizing the global network response via Eq. (6), we anticipate that the tuning of individual covariance matrix elements can provide a powerful technique for the fine-grained control of specific dynamical properties. Perhaps most importantly, however, due to its generic mathematical formulation, the LRO scheme can be applied to any dynamical system that can be linearized near a stable fixed point. This promises exciting future possibilities for the inverse design of complex static and dynamic target functionalities in a wide range of systems, from amorphous photonic crystals [50] and DNA origami structures [51,52] to passive [53] and active [54] topolectrical circuits.

ACKNOWLEDGMENTS

This work was supported by the Solomon Buchsbaum Research Fund of the Massachusetts Institute of Technology.

APPENDIX: METHODS

1. Gradient-based optimization

We employed the standard L-BFGS-B bound-constrained quasi-Newton algorithm [55]. In the numerical examples, stiffness values k_e were optimized over the interval $[0.1, 1]$.

2. Randomized topology

Networks with randomized topology were constructed by first distributing points $\mathbf{x}_i$ in the periodic unit cell uniformly at random, and then locally minimizing the potential function $V = \sum_{i \neq j} d(\mathbf{x}_i, \mathbf{x}_j)^{-1}$, where the distance $d(\mathbf{x}_i, \mathbf{x}_j) = \min_{\mathbf{m}} \|\mathbf{x}_i - \mathbf{x}_j + \mathbf{m}\|$ for lattice vectors $\mathbf{m}$. The basic unit-cell points were copied into the directly adjacent unit cells, and a Delaunay triangulation was calculated to obtain the network topology and unit vectors along the bonds. Equivalent points were identified in the basic unit cell, and the adjacent unit cells were deleted.

3. Spectra of deformed networks

The spectrum of an elastic network described by Eq. (1) is found by linearizing the elastic energy to

$$V = \frac{1}{2} \sum_e k_e (\hat{\mathbf{b}}_e \cdot \Delta\mathbf{u}_e)^2, \tag{A1}$$

where k_e are the spring stiffnesses of spring e, $\hat{\mathbf{b}}_e$ is the unit vector pointing along $e = (ij)$, and $\Delta\mathbf{u}_e = \mathbf{u}_i - \mathbf{u}_j$ for

the small displacements $\mathbf{x}_i = \mathbf{x}_i^{(0)} + \mathbf{u}_i$ from the equilibrium positions $\mathbf{x}_i^{(0)}$. To linear order, a global deformation is then defined by

$$\mathbf{x} \to (\mathbb{1} + \eta)(\mathbf{x}^{(0)} + \mathbf{u}) \approx \mathbf{x}^{(0)} + \eta\mathbf{x}^{(0)} + \mathbf{u}, \tag{A2}$$

where the $d \times d$ matrix η encodes the global deformation. Plugging this into Eq. (A1) and minimizing with respect to $\mathbf{u}$, we obtain the new equilibrium positions of the network nodes under the global deformation.

The spectrum of the deformed network is then found by expanding (A1) around the new equilibrium positions $\mathbf{x}_{\text{def}} = \mathbf{x}^{(0)} + \eta\mathbf{x}^{(0)} + \mathbf{u}_{\text{def}}$. Up to a constant, we obtain

$$V_{\text{def}} = \frac{1}{2}\sum_e k_e\left[\frac{\ell_e^{(0)}}{\tilde{\ell}_e}(\tilde{\mathbf{b}}_e \cdot \Delta\mathbf{v}_e)^2 + \left(1 - \frac{\ell_e^{(0)}}{\tilde{\ell}_e}\right)(\Delta\mathbf{v}_e)^2\right], \tag{A3}$$

where the tilde denotes a quantity in the deformed equilibrium, and $\mathbf{v}_i$ are the small displacements around the deformed equilibrium.

4. Finite-element calculations

We used MATLAB 2018b's `createpde` command in the `structural` mode for solid modal analysis. The meshes were generated using the default parameters, only the maximum mesh size was set to `0.005`. The material properties were set for Styrodur (BASF AG, Ludwigshafen, Germany), a polymer foam with Young's modulus $Y = 2 \times 10^7$ Pa, Poisson's ratio $\nu = 0.4$, and density $\rho = 33$ kg/m^3. To compare the results of 3D finite-element (FE) calculations to our 2D network model, for each mode with x, y, z components $(\mathbf{u}_x, \mathbf{u}_y, \mathbf{u}_z)$ we computed the in-plane contribution $f_{xy}^2 = (\|\mathbf{u}_x\|^2 + \|\mathbf{u}_y\|^2)/(\|\mathbf{u}_x\|^2 + \|\mathbf{u}_y\|^2 + \|\mathbf{u}_z\|^2)$, and we discarded all modes with $f_{xy} < 0.5$. Additional details of the mapping between the 2D network model and the 3D FE model are provided in Ref. [38].

[1] S. A. Cummer, J. Christensen, and A. Alù, Nat. Rev. Mater. **1**, 16001 (2016).
[2] S. Zhang, C. Xia, and N. Fang, Phys. Rev. Lett. **106**, 024301 (2011).
[3] T. Brunet, A. Merlin, B. Mascaro, K. Zimny, J. Leng, O. Poncelet, C. Aristégui, and O. Mondain-Monval, Nat. Mater. **14**, 384 (2014).
[4] R. Martínez-Sala, J. Sancho, J. V. Sánchez, V. Gómez, J. Llinares, and F. Meseguer, Nature (London) **378**, 241 (1995).
[5] N. Bhattacharjee, A. Urrios, S. Kang, and A. Folch, Lab Chip **16**, 1720 (2016).
[6] T. Bückmann, N. Stenger, M. Kadic, J. Kaschke, A. Frölich, T. Kennerknecht, C. Eberl, M. Thiel, and M. Wegener, Adv. Mater. **24**, 2710 (2012).
[7] K. Bertoldi, V. Vitelli, J. Christensen, and M. van Hecke, Nat. Rev. Mater. **2**, 17066 (2017).
[8] G. Ma, C. Fu, G. Wang, P. del Hougne, J. Christensen, Y. Lai, and P. Sheng, Nat. Commun. **7**, 13536 (2016).
[9] P. A. Deymier, *Acoustic Metamaterials and Phononic Crystals*, Vol. 173 of Springer Series in Solid-State Sciences (Springer, Berlin, 2013).
[10] R. Süsstrunk and S. D. Huber, Proc. Natl. Acad. Sci. USA **113**, E4767 (2016).
[11] Z. Wang, Q. Zhang, K. Zhang, and G. Hu, Adv. Mater. **28**, 9857 (2016).
[12] J. Cha and C. Daraio, Nat. Nanotechnol. **13**, 1016 (2018).
[13] K. Bertoldi and M. C. Boyce, Phys. Rev. B **77**, 052105 (2008).
[14] G. Gui, J. Li, and J. Zhong, Phys. Rev. B **78**, 075435 (2008).
[15] L. Wang and K. Bertoldi, Int. J. Solids. Struct. **49**, 2881 (2012).
[16] O. Sigmund and J. Sondergaard Jensen, Philos. Trans. R. Soc. A **361**, 1001 (2003).
[17] M. P. Bendsøe and O. Sigmund, *Topology Optimization Theory, Methods and Applications*, 2nd ed. (Springer, New York, 2003), p. 370.
[18] K. Diest, *Numerical Methods for Metamaterial Design (Topics in Applied Physics)* (Springer, Heidelberg, 2013).
[19] M. C. Rechtsman, H.-C. Jeong, P. M. Chaikin, S. Torquato, and P. J. Steinhardt, Phys. Rev. Lett. **101**, 073902 (2008).
[20] W. Man, M. Florescu, K. Matsuyama, P. Yadak, G. Nahal, S. Hashemizad, E. Williamson, P. Steinhardt, S. Torquato, and P. Chaikin, Opt. Express **21**, 19972 (2013).
[21] M. Florescu, S. Torquato, and P. J. Steinhardt, Proc. Natl. Acad. Sci. USA **106**, 20658 (2009).
[22] D. Mousanezhad, S. Babaee, R. Ghosh, E. Mahdi, K. Bertoldi, and A. Vaziri, Phys. Rev. B **92**, 104304 (2015).
[23] L. M. Nash, D. Kleckner, A. Read, V. Vitelli, A. M. Turner, and W. T. M. Irvine, Proc. Natl. Acad. Sci. USA **112**, 14495 (2015).
[24] P. Wang, L. Lu, and K. Bertoldi, Phys. Rev. Lett. **115**, 104302 (2015).
[25] H. Men, K. Y. K. Lee, R. M. Freund, J. Peraire, and S. G. Johnson, Opt. Express **22**, 22632 (2014).
[26] R. H. Olsson III and I. El-Kady, Meas. Sci. Technol. **20**, 012002 (2009).
[27] C. Goffaux and J. P. Vigneron, Phys. Rev. B **64**, 075118 (2001).
[28] A. Agarwala and V. B. Shenoy, Phys. Rev. Lett. **118**, 236402 (2017).
[29] N. P. Mitchell, L. M. Nash, and W. T. M. Irvine, Phys. Rev. B **97**, 100302(R) (2018).
[30] L. Yan, R. Ravasio, C. Brito, and M. Wyart, Proc. Natl. Acad. Sci. USA **114**, 2526 (2017).
[31] D. R. Reid, N. Pashine, J. M. Wozniak, H. M. Jaeger, A. J. Liu, S. R. Nagel, and J. J. de Pablo, Proc. Natl. Acad. Sci. USA **115**, E1384 (2018).
[32] H. Flechsig, Biophys. J. **113**, 558 (2017).
[33] J. W. Rocks, N. Pashine, I. Bischofberger, C. P. Goodrich, A. J. Liu, and S. R. Nagel, Proc. Natl. Acad. Sci. USA **114**, 2520 (2017).
[34] C. P. Goodrich, A. J. Liu, and S. R. Nagel, Phys. Rev. Lett. **114**, 225501 (2015).
[35] J. W. Rocks, H. Ronellenfitsch, A. J. Liu, S. R. Nagel, and E. Katifori, Proc. Natl. Acad. Sci. USA **116**, 2506 (2019).

[36] J. S. Jensen, J. Sound. Vib. **266**, 1053 (2003).
[37] T. C. Lubensky, C. L. Kane, X. Mao, A. Souslov, and K. Sun, Rep. Prog. Phys. **78**, 073901 (2015).
[38] See Supplemental Material at http://link.aps.org/supplemental/10.1103/PhysRevMaterials.3.095201 for movies and additional calculation details.
[39] W. Setyawan and S. Curtarolo, Comput. Mater. Sci. **49**, 299 (2010).
[40] H. Men, N. Nguyen, R. Freund, P. Parrilo, and J. Peraire, J. Comput. Phys. **229**, 3706 (2010).
[41] H. Ronellenfitsch, J. Dunkel, and M. Wilczek, Phys. Rev. Lett. **121**, 208301 (2018).
[42] K. Miettinen, *Nonlinear Multiobjective Optimization*, Vol. 12 of International Series in Operations Research & Management Science (Springer, Boston, MA, 1998).
[43] B. Audoly and Y. Pomeau, *Elasticity and Geometry* (Oxford University Press, Oxford, 2010).
[44] M. Bergou, M. Wardetzky, S. Robinson, B. Audoly, and E. Grinspun, ACM Trans. Graph. **27**, 63 (2008).
[45] C. L. Kane and T. C. Lubensky, Nat. Phys. **10**, 39 (2014).
[46] A. Souslov, B. C. van Zuiden, D. Bartolo, and V. Vitelli, Nat. Phys. **13**, 1091 (2017).
[47] N. P. Mitchell, L. M. Nash, D. Hexner, A. M. Turner, and W. T. M. Irvine, Nat. Phys. **14**, 380 (2018).
[48] Y.-T. Wang, P.-G. Luan, and S. Zhang, New J. Phys. **17**, 073031 (2015).
[49] M. Xiao, G. Ma, Z. Yang, P. Sheng, Z. Q. Zhang, and C. T. Chan, Nat. Phys. **11**, 240 (2015).
[50] J. Ricouvier, P. Tabeling, and P. Yazhgur, Proc. Natl. Acad. Sci. USA **116**, 9202 (2019).
[51] M. Bathe and P. W. Rothemund, MRS Bull. **42**, 882 (2017).
[52] W. Sun, E. Boulais, Y. Hakobyan, W. L. Wang, A. Guan, M. Bathe, and P. Yin, Science **346**, 1258361 (2014).
[53] C. H. Lee, S. Imhof, C. Berger, F. Bayer, J. Brehm, L. W. Molenkamp, T. Kiessling, and R. Thomale, Commun. Phys. **1**, 39 (2018).
[54] T. Kotwal, H. Ronellenfitsch, F. Moseley, A. Stegmaier, R. Thomale, and J. Dunkel, arXiv:1903.10130.
[55] R. H. Byrd, P. Lu, J. Nocedal, and C. Zhu, SIAM J. Sci. Comput. **16**, 1190 (1995).